# Tin sulfide chalcogel derived SnS$_x$ for CO$_2$ electroreduction

Published as part of the Virtual Special Issue "Mercouri G. Kanatzidis at 65"

Jingwen Bai[1,2†], Lijun Yang[2†], Yuanyuan Zhang[1,2], Xiaofu Sun[3] and Jian Liu[1,2*]

A new class of aerogels based exclusively on metal chalcogenide frameworks have been developed, opening up a series of novel properties and applications. Further expanding the application of such chalcogels in electrocatalytic CO$_2$ reduction is of significance for mitigating the rise of atmospheric CO$_2$ concentration. Herein, the tin sulfide chalcogel was employed as a pre-catalyst for the construction of efficient electrocatalysts for CO$_2$ reduction. SnS$_{0.09}$ and SnS$_{0.55}$ supported on carbon cloth (SnS$_{0.09}$/CC and SnS$_{0.55}$/CC) were obtained with different amounts of sulfur by cyclic voltammetry activation of the tin sulfide chalcogel at different potential intervals. Compared with SnS$_{0.09}$/CC, SnS$_{0.55}$/CC with higher S contents exhibited a higher formate Faraday efficiency of 93.1% at −1.1 V verse reversible hydrogen electrode, and the partial current density of formate was 28.4 mA/cm^2. The difference in performance between SnS$_{0.09}$/CC and SnS$_{0.55}$/CC could be attributed to the varying sulfur contents which could favor the formation of formate.
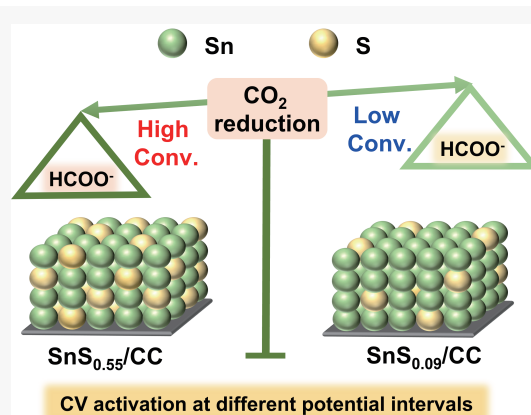
Chalcogels are a newly emerging class of highly porous aerogels based exclusively on metal chalcogenide frameworks.[1–4] Chalcogels have the general properties of metal chalcogenide compounds, such as unique pore structures, suitable band gaps, semiconductor properties and so on.[1,5–7] Due to the abundance of soluble chalcogenide clusters and metal ions, the properties of chalcogels could be tuned through carefully choosing the appropriate anions and cations.[1,5,8,9] Besides, compared with metal chalcogenide compounds, the one-pot synthesis of chalcogels was usually accomplished at ambient conditions.[6,10,11] These features allow the chalcogels to show potential applications in catalysis, gas separation and adsorption, environmental remediation, and so on.[3,4,8,12–18]

Studies of the chalcogels in electrocatalytic applications have focused mainly on electrocatalytic hydrogen evolution reactions,[19–21] whereas it is equally necessary to extend to CO$_2$ reduction reaction (CO$_2$RR). As well known, with the combustion of fossil fuels, the continuous rise of atmospheric CO$_2$ concentration poses a serious threat to the environment and climate. In order to mitigate atmospheric CO$_2$ concentration, electrocatalytic CO$_2$RR is an appealing and sustainable strategy, as the electricity can be provided by abundant and renewable energy sources.[22–24] The feasibility of chalcogels in electrocatalytic CO$_2$RR has been demonstrated by Kanatzidis et al. using biomimetic chalcogels comprised of Na$_4$Sn$_2$S$_6$·14H$_2$O and (Ph$_4$P)$_2$[Fe$_4$S$_4$Cl$_4$].[11] However, the active sites of such catalysts were not very clear. Therefore, further exploring the study of chalcogels in electrocatalytic CO$_2$RR and establishing the structure-activity relationship are of great significance.

Among the reported chalcogels, the tin sulfide chalcogel (SnS$_x$) has a simple composition consisting of Sn^{2+} and [SnS$_4$]$^{4-}$, which is more favorable for establishing the relationship between composition and reaction performance. Tin sulfide has been widely investigated in the field of electrocatalysis.[25–30] In addition, tin-based materials have been widely employed as electrocatalysts for CO$_2$RR to produce formate.[29,31–37] Among the various liquid products, formate is considered to be one of the most economically feasible products, which is widely used as an important raw material in the chemical industries and a promising carrier for hydrogen storage.[38–41] Therefore, SnS$_x$ chalcogel was tentatively employed as the starting material for construction of the efficient electrocatalyst for CO$_2$RR.

[1] *College of Materials Science and Engineering, Qingdao University of Science and Technology, Qingdao 266042, China*

[2] *Qingdao Institute of Bioenergy and Bioprocess Technology, Chinese Academy of Sciences, Shandong Energy Institute, Qingdao 266101, China*

[3] *Beijing National Laboratory for Molecular Sciences, CAS Key Laboratory of Colloid and Interface and Thermodynamics, CAS Research/Education Center for Excellence in Molecular Sciences, Institute of Chemistry, Chinese Academy of Sciences, Beijing 100190, China*

* Corresponding author, E-mail: liujian@qibebt.ac.cn

In our study, we found that SnS_x was unstable and underwent morphological and composition changes after cyclic voltammetry (CV) activation. Such changes prompted us to employ the chalcogel SnS_x as a pre-catalyst for further study. The "real" catalysts after CV activation at different potential intervals were termed as $SnS_{0.09}$/CC and $SnS_{0.55}$/CC, respectively. According to the characterization of the energy-dispersive X-ray spectroscopy (EDS) and X-ray photoelectron spectroscopy (XPS), the S contents were found to be decreased for both $SnS_{0.09}$/CC and $SnS_{0.55}$/CC after CV activation, and the latter had higher S contents than the former counterpart. At −1.1 V verse reversible hydrogen electrode (vs. RHE), $SnS_{0.55}$/CC demonstrated a higher formate Faraday efficiency of 93.1% and the formate partial current density of 28.4 mA/cm², surpassing those of $SnS_{0.09}$/CC. The phenomenon was attributed to the higher S contents in $SnS_{0.55}$/CC, which facilitated the formation of formate. The current study could shed light on the construction of metal sulfide electrocatalysts by in-situ electrochemical activation.

Materials and methods

Chemicals and materials

All the reagents were purchased commercially and used without further purification. Sodium sulfide nonahydrate ($Na_2S·9H_2O$), methanol, ethanol, formamide, potassium bicarbonate ($KHCO_3$) were purchased from Sinopharm Chemical Reagent Co. Ltd.. Tin (IV) chloride pentahydrate ($SnCl_4·5H_2O$) was purchased from Shanghai Aladdin Biochemical Technology Co. Ltd.. Tin (II) acetate ($Sn(OAc)_2$) was purchased from Energy Chemical Co. Ltd.. Nafion 117 containing solution was purchased from Sigma Aldrich.

Synthesis of $Na_4SnS_4·14H_2O$

$Na_2S·9H_2O$ (120 mmol) was dissolved in 100 mL H_2O with stirring. Then, $SnCl_4·5H_2O$ (30 mmol) was dissolved in 5 mL H_2O and added dropwise to the $Na_2S·9H_2O$ solution with continuous stirring. The solution was kept at 45 °C for 8 h and then added to 400 mL methanol. The flask was placed in a refrigerator for 48 h. Precipitated white crystal of $Na_4SnS_4·14H_2O$ was washed with EtOH and dried under vacuum for 24 h.

Synthesis of tin sulfide chalcogel (SnS_x)

Tin sulfide chalcogel (SnS_x) was synthesized by using a modification of the literature method as follows[42]: $Na_4SnS_4·14H_2O$ (0.2 mmol) and $Sn(OAc)_2$ (0.4 mmol) were dissolved in a total 8 mL of formamide in two separate vials. The $Sn(OAc)_2$ solution was added very slowly to the $Na_4SnS_4·14H_2O$ solution with vigorous stirring. Small, yellowish-orange particles appeared upon the addition of a drop of $Sn(OAc)_2$ solution, but they disappeared with shaking. Addition of the $Sn(OAc)_2$ was followed by vigorous shaking. Then, the vial was placed in an oil bath (60 °C) for 7 days. The remaining formamide was decanted and the gel was subsequently washed with water and ethanol over 3 days and finally dried through freeze-drying, resulting in the SnS_x powders.

Electrode preparation

10 mg of SnS_x, 3 mg of carbon black, and 50 μL of Nafion solution (5 wt%) were dispersed in 1 mL of ethanol via sonication for 30 min to form a homogeneous ink. Then, the as-prepared catalyst ink was drop-cast onto a piece of cleaned carbon cloth with an area of $1 × 1$ cm² to form the electrode with catalyst loading of 1 mg/cm². The prepared electrodes were dried under ambient environment.

Electrochemical activation of SnS_x in different potential regions

The as-obtained SnS_x electrodes were electro-activated by 20-segment consecutive CV scans through two different potential intervals in CO_2-saturated 0.5 M $KHCO_3$ with a scan rate of 50 mV/s. According to the quantitative analysis of XPS, the working electrode obtained by electrochemical activation from 0.16 V to −1.54 V vs. RHE was named $SnS_{0.09}$/CC. The working electrode obtained by electrochemical activation from 0.76 V to −1.54 V vs. RHE was named $SnS_{0.55}$/CC.

Electrochemical measurements

All electrochemical CO_2 reduction experiments was conducted in a three-electrode system in a gas-tight H-cell (separated by Nafion 117) containing 180 mL of 0.5 M $KHCO_3$ electrolyte at room temperature and under atmospheric pressure. $SnS_{0.09}$/CC and $SnS_{0.55}$/CC were used directly as the working electrodes. Ag/AgCl (with saturated KCl as the filling solution) and platinum mesh were used as the reference and counter electrodes, respectively. The potentials were controlled by a CHI660E electrochemical station. Electrode potentials were converted to RHE scale according to the Nernst equation: on: on: on: $E_{RHE} = E_{Ag/AgCl} + 0.197 V + 0.0591 × pH$. The pH values of N_2- and CO_2-saturated 0.5 M $KHCO_3$ electrolyte were 8.52 and 7.70, respectively. After CO_2 was purged into the $KHCO_3$ solution for at least 30 min to saturate the electrolyte, electroreduction of CO_2 was investigated for 1 h at each applied potential by the controlled potential electrolysis method. The average mass flowrate of CO_2 (99.999%) was controlled at 25 mL/min by a mass flow controller (YJ-700CF) at the inlet of the electrochemical cell. The gaseous products of CO_2 electrocatalytic reduction were monitored by an on-line gas chromatography (GC) (GC9790plus, Fuli Instruments) equipped with the flame ionization detector (FID) and thermal conductivity detector (TCD). H_2 and CO concentrations were analyzed by the TCD and FID detectors, respectively. The $KHCO_3$ solution after electrolysis was collected and analyzed on an ion chromatograph (863 Basic IC plus, Metrohm, Switzerland) equipped with a MetrosepA Supp 4-250/4.0 column to quantify liquid products (formate). Faradaic efficiencies (FE) of formate, CO and H_2 were calculated by the equation: FE (%) = nFz/Q, where n represents the total number of moles of formate, CO and H_2 production, which were measured by ion chromatograph and GC; F represented Faraday constant (96485); z represented the number of electrons required to form formate, CO and H_2 from CO_2; and the Q corresponded to the amount of cumulative charge in the process of CO_2 reduction, which was provided by the electrochemical workstation.

The linear scanning voltammetry (LSV) curves of $SnS_{0.09}$/CC and $SnS_{0.55}$/CC were carried out in CO_2-saturated or N_2-saturated 0.5 M $KHCO_3$ with the scan rate of 5 mV/s based on the above electrolysis cell. Double-layer capacitance (Cdl) was determined by measuring the capacitive current associated with double-layer charging from the scan-rate dependence of CV. The CV ranged from 0.31 V to 0.41 V vs. RHE. The Cdl was es-

timated by plotting the ΔJ ($\Delta J = j_a - j_c$) at 0.36 V vs. RHE against the scan rates, in which the j_a and j_c were the anodic and cathodic current density, respectively. The slope was twice that of the Cdl values. The electrochemical impedance spectra of the SnS$_{0.09}$/CC and SnS$_{0.55}$/CC were recorded at -0.8 V vs. RHE in CO$_2$-saturated 0.5 M KHCO$_3$ electrolyte with an amplitude of e frequency range is from 0.1 Hz to 100000 Hz.

Characterizations

Scanning electron microscopy (SEM) and EDS was performed on a JEOL JSM-6700F scanning electron microscope equipped with an energy dispersive X-ray spectroscopy detector. Transmission Electron Microscope (TEM) and High-Resolution Transmission Electron Microscopy (HRTEM) were carried out on a JEOL JEM-2100Plus transmission electron microscope with an acceleration voltage of 200 kV. Powder X-ray diffraction (XRD) patterns were recorded by using a Rigaku Ultima IV diffractometer (Cu Kα radiation, λ=1.5418 Å) with an operating voltage of 40 kV and a current of 44 mA. XPS measurements were carried out on a Thermo Scientific K-Alpha system, with a 400 μm spot size, 50 eV pass energy and energy steps of 0.1 eV, and aluminum anode X-ray excitation.

Results

Preparation and characterization of tin sulfide chalcogel (SnS$_x$)

In the present study, the SnS$_x$ chalcogel was synthesized by the metathesis reaction between Na$_4$SnS$_4$·14H$_2$O and Sn(OAc)$_2$. As shown in Fig. S1a, formamide solutions of two reactants were slowly mixed, and the resultant solution was kept at 60 °C for gelation. The SnS$_x$ powders were obtained after the solvent exchange and freeze drying (Fig. S1b and S1c). SEM (Fig. 1a) and TEM (Fig. 1b) images showed the formation of micron-sized particles by aggregation of nanoparticles. HRTEM image reflected that SnS$_x$ powders were crystalline with an interplanar distance of lattice fringes of 0.34 nm, which ascribed to the (201) plane of SnS and the (101) plane of Sn$_2$S$_3$ (Fig. 1c). EDS spectra showed that Sn, S,

Na and O presented in the SnS$_x$ powders (Fig. S2). The small amount of Na originated from the reaction feedstock residue and the small amount of O may be due to the exposure of the catalyst to air. As indicated by elemental mapping, S and Sn elements were distributed homogeneously among SnS$_x$ particles (Fig. S3). SnS$_x$ consisted of SnS and Sn$_2$S$_3$ according to the XRD pattern, and the sharp diffraction peaks indicated the crystallinity of SnS$_x$, which also corresponded to the results of HRTEM (Fig. 1d). XPS survey spectra further confirmed the chemical composition of SnS$_x$ (Fig. S4). As evidenced by XPS spectra of Sn 3d, Sn presented in the form of Sn^{2+} (494.7 eV and 486.3 eV) and Sn^{4+} (495.5 eV and 487.1 eV).[37,43] Two characteristic peaks at 162.7 eV and 161.5 eV were assigned to S 2$p_{1/2}$ and S 2$p_{3/2}$ of SnS$_x$, respectively (Fig. 1f).[30,43]

Electrochemical activation of SnS$_x$ in different potential regions

SnS$_x$ powders were loaded on a 1 × 1 cm^2 area of carbon cloth (SnS$_x$/CC), which was used as a working electrode for electrochemical CO$_2$RR. CV scans were usually carried out prior to the performance tests to activate the electrodes. We applied 10 cycles of CV scans before other tests (scan rate: 50 mV/s). Typical CV curves are shown in Fig. S5b. A reduction peak at -0.35 V vs. RHE and an oxidation peak at 0.25 V vs. RHE emerged in the second voltammetric cycle (this process was poorly defined in the first voltammetric cycle), suggesting the occurrence of reduction and oxidation for SnS$_x$.[44,45] By adopting different potential intervals for activation of the electrodes, SnS$_x$ would undergo different redox processes to obtain electrocatalysts with different morphologies and components. According to the atom ratio of Sn and S obtained by XPS quantitative analysis (Fig. S9 and Table S2), the electrodes activated at two different potential intervals were named as SnS$_{0.09}$/CC (0.16 V~−1.54 V vs. RHE) and SnS$_{0.55}$/CC (0.76 V~−1.54 V vs. RHE), respectively (Fig. S5a and S5b). The electrode SnS$_{0.09}$/CC underwent only reduction, and SnS$_{0.55}$/CC underwent both reduction and oxidation. From the optical photographs in Fig. S5c-S5e, gray-white substances appeared on the surface of both electrodes after CV,
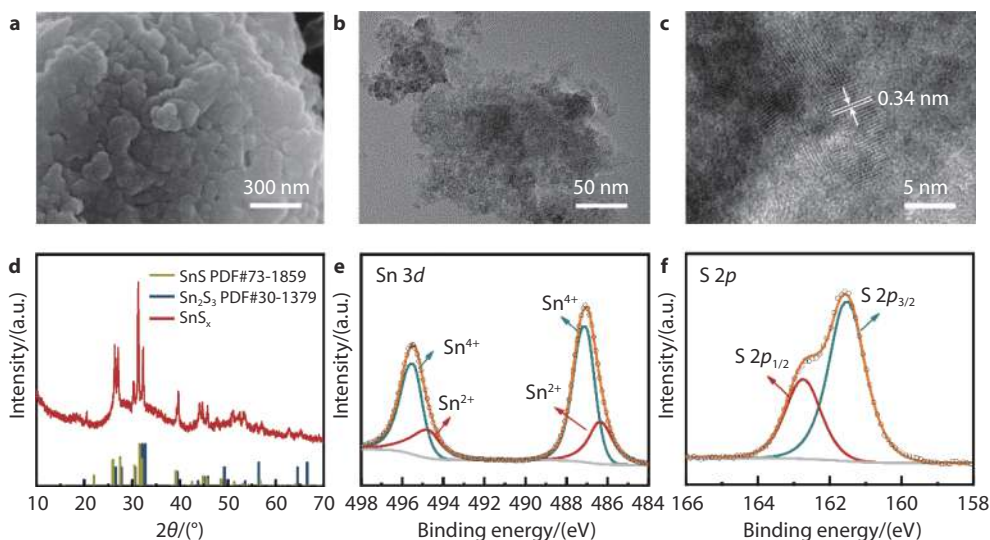

Fig. 1 **a** SEM image, **b** TEM image, **c** HRTEM image, **d** XRD patterns, **e** Sn 3d XPS spectra and **f** S 2p XPS spectra of SnS$_x$ powders.

further confirming the transformation of substances in the CV process. $SnS_{0.09}$/CC produced more gray-white materials than $SnS_{0.55}$/CC, indicating that different potential ranges of CV activation had effects on SnS_x conversion in electrochemical processes. The effect of activation using different potential intervals on the morphology of the electrocatalysts was confirmed by SEM. As shown by Fig. 2a, S6a and S6b, the pre-catalyst SnS_x/CC consisted of numerous nanoparticles that were composed of smaller ones. The average size of SnS_x/CC particles was 69.3 ± 6 nm. Compared to SnS_x/CC, larger particles with the average size of 186 ± 4 nm appeared on the $SnS_{0.09}$/CC electrode. In contrast, the particles did not grow significantly on the $SnS_{0.55}$/CC electrode, with the average size of 73.3 ± 9 nm (Fig. 2b, 2c, and S6c-S6f). The EDS mapping patterns of Sn and S in the three electrodes reflected the different S contents (Fig. S7). This feature was further evident by the elemental content analysis of the EDS (Fig. S8 and Table S1). The Sn/S atomic ratios of SnS_x/CC, $SnS_{0.09}$/CC and $SnS_{0.55}$/CC were 1/1.68, 1/0.09 and 1/0.47, respectively, which were consistent with the XPS results. It indicated that the S content of both electrocatalysts decreased after CV activation, and $SnS_{0.55}$/CC contained more S elements than $SnS_{0.09}$/CC. The above results could illustrate that different activation potential intervals in CV activation affect the morphology and composition of the electrocatalysts.

To further investigate the composition and structure of $SnS_{0.09}$/CC and $SnS_{0.55}$/CC, we carried out a series of characterizations including XRD and XPS measurements. As evidenced by XRD patterns (Fig. 2d), $SnS_{0.09}$/CC was consisted of metallic Sn, SnS and Sn_2S_3, indicating the reduction of SnS_x to metallic Sn occurred at a potential interval (0.16 V~−1.54 V) vs. RHE) with a small amount of unconverted SnS_x. In contrast, $SnS_{0.55}$/CC just showed peaks with weak intensities assigning to Sn, SnS and Sn_2S_3, respectively. The reason was ascribed to the fact that SnS_x constantly underwent reduction and oxidation during electrochemical activation in the potential region of 0.76~−1.54 V vs. RHE. As evidenced by the Sn 3d XPS spectra of the three electrodes, $SnS_{0.09}$/CC had the appearance of

the peak of Sn^0, whereas this phenomenon was not observed for $SnS_{0.55}$/CC (Fig. 2e).[37,46] Fig. 2f showed the S 2p XPS spectra of the three electrodes. Two characteristic peaks at 168.4 eV and 169.8 eV were assigned to sulfate/nafion.[47,48] Two peaks at 162.7 eV and 161.5 eV attributed to S $2p_{1/2}$ and S $2p_{3/2}$ of SnS_x, respectively. Fig. 2e and 2f also reflected that peaks shift of Sn and S in the XPS for $SnS_{0.09}$/CC and $SnS_{0.55}$/CC. Relative to SnS_x/CC, the XPS peaks of Sn for $SnS_{0.09}$/CC and $SnS_{0.55}$/CC shifted to lower binding energies, whereas the XPS peaks of S shifted to higher binding energies, which could be attributed to the electron transfer from S to Sn. The different degree of peaks shift could further infer that the different potential intervals in CV activation affected the electron transfer between Sn and S, which changed the electronic structure of the Sn sites and thus may influence the interaction between catalysts and CO_2.[29]

Scheme 1 demonstrated the in-situ conversion processes of the pre-catalyst SnS_x/CC through different potential intervals in electrochemical activation. The CV curves of $SnS_{0.99}$/CC showed only one reduction peak at −0.35 V vs. RHE, indicating the occurrence of only reduction reactions. Most of the SnS_x was converted to metallic Sn, and a very small amount of S remained. In this conversion, the nanoparticles on the $SnS_{0.99}$/CC electrode became larger. For $SnS_{0.55}$/CC, SnS_x was first converted to metallic Sn and S ions entered the electrolyte before the oxidation process occurred with S ions. During electrochemical activation, $SnS_{0.55}$/CC has been following this redox process. Thus, compared to $SnS_{0.99}$/CC, $SnS_{0.55}$/CC contained more S and smaller particles. Through the selection of different potential intervals in CV activation, the pre-catalyst transformed to two electrocatalysts with different particle sizes and composition, which was especially reflected in the atom ratio of Sn to S. The thus obtained catalysts feature different active sites, which were used in the electrocatalytic CO_2RR.

Electrochemical CO_2RR performance of the $SnS_{0.09}$/CC and $SnS_{0.55}$/CC
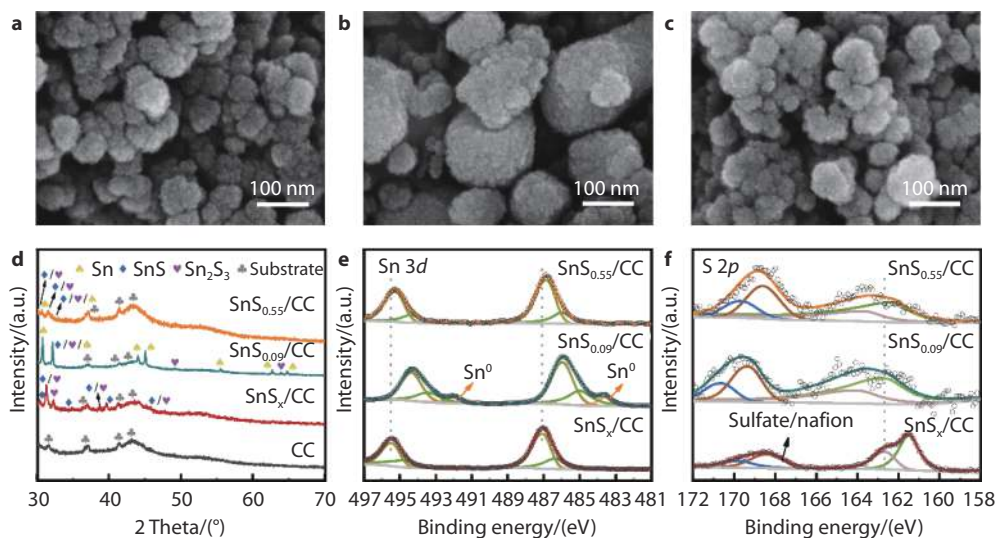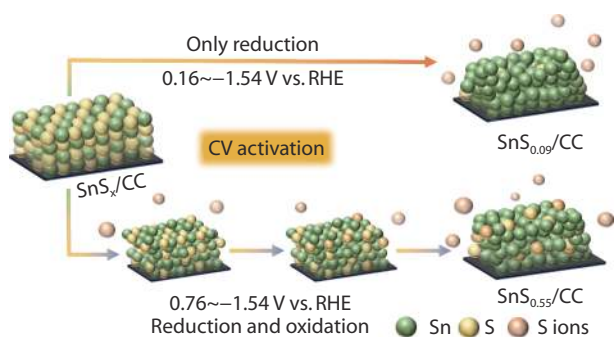
Electrocatalytic CO_2RR performance of the $SnS_{0.09}$/CC and

Fig. 2 SEM images of **a** SnS_x/CC, **b** $SnS_{0.09}$/CC and **c** $SnS_{0.55}$/CC; **d** XRD patterns, **e** Sn 3d XPS spectra and **f** S 2p XPS spectra of SnS_x/CC, $SnS_{0.09}$/CC and $SnS_{0.55}$/CC.

Scheme 1 In-situ electrochemical activation of SnS$_x$ by different potential regions in CV activation.

SnS$_{0.55}$/CC samples were evaluated in a gas-tight H-cell containing 180 mL of CO$_2$-saturated 0.5 M KHCO$_3$ electrolyte, which was separated by a proton exchange membrane (Fig. S10). Fig. 3a showed LSV curves of the SnS$_{0.09}$/CC and SnS$_{0.55}$/CC in CO$_2$- and N$_2$-saturated 0.5 M KHCO$_3$. As shown in the inset of Fig. 3a, the reduction peaks were observed in LSV curves, indicating that the self-reduction of SnS$_{0.09}$/CC and SnS$_{0.55}$/CC occurred during the LSV test. Both SnS$_{0.09}$/CC and SnS$_{0.55}$/CC exhibited higher current densities in CO$_2$- than in N$_2$-saturated electrolyte, implying their promising applications in CO$_2$ electroreduction. Furthermore, SnS$_{0.55}$/CC exhibited a larger current density than that of SnS$_{0.09}$/CC in CO$_2$-saturated electrolyte, suggesting SnS$_{0.55}$/CC was more active for electrocatalytic CO$_2$RR. At potentials of −1.0 V and −1.1 V vs. RHE, SnS$_{0.55}$/CC exhibited considerable current densities of 21.8 mA/cm^2 and 30.5 mA/cm^2, respectively. To further evaluate CO$_2$RR activity and selectivity, chronoamperometry tests were conducted at different potentials. Quantified by gas chromatography and ion chromatography analysis, the cata-

lytic products in CO$_2$ electroreduction included formate (HCOO$^-$), CO, and H$_2$ over the SnS$_{0.09}$/CC and SnS$_{0.55}$/CC. As shown in Fig. 3b and S11, formate was the major product over the whole potential range, while CO and H$_2$ were the minor products for the SnS$_{0.09}$/CC and SnS$_{0.55}$/CC. SnS$_{0.55}$/CC exhibited higher selectivity to formate, achieving a formate FE of 93.1% at −1.1 V vs. RHE, whereas the maximum formate FE of SnS$_{0.09}$/CC was 86.8% (Fig. 3b, S11 and 12c). Compared with SnS$_{0.55}$/CC, the lower selectivity for formate of SnS$_{0.09}$/CC was attributed to its preference for hydrogen evolution reactions (Fig. 3b, S11 and 12a). There was no significant difference in FE for CO production between the SnS$_{0.09}$/CC and SnS$_{0.55}$/CC (Fig. 3b, S11, 12a and S12b). We further calculated the partial current density (J) of the SnS$_{0.09}$/CC and SnS$_{0.55}$/CC at all of applied potentials (Fig. S13). At −1.1 V vs. RHE, SnS$_{0.55}$/CC exhibited a J$_{HCOO^-}$ of 28.4 mA/cm^2, which was larger than that of SnS$_{0.09}$/CC (22.1 mA/cm^2, Fig. 3c). J$_{H2}$ of SnS$_{0.55}$/CC was slightly less than that of SnS$_{0.09}$/CC, and J$_{CO}$ of SnS$_{0.55}$/CC was slightly higher than that of SnS$_{0.09}$/CC (Fig. S14). The stability of the SnS$_{0.09}$/CC and SnS$_{0.55}$/CC in CO$_2$RR were examined at a constant applied potential of −1.1 V vs. RHE for 12 h (Fig. S15). Both SnS$_{0.09}$/CC and SnS$_{0.55}$/CC exhibited steady FEs for formate of about 83.3% and 90.4%, respectively. The current densities of both electrodes showed a trend of increasing with time, in which the current densities increasing more rapidly in the first 2 hours. After 12 hours of stability testing, both electrodes became whiter in color and the particle sizes became larger (Fig. S16 and S17). The EDS and the XPS quantitative analysis results reflected that after 12 hours of reaction, S content among the two electrodes got decreased (Fig. S16g and S18-S20), and similar Sn/S atom ratio was found for SnS$_{0.09}$/CC-12 h and SnS$_{0.55}$/CC-12 h (Table S3 and S4). XRD patterns and the Sn 3d XPS spectra of
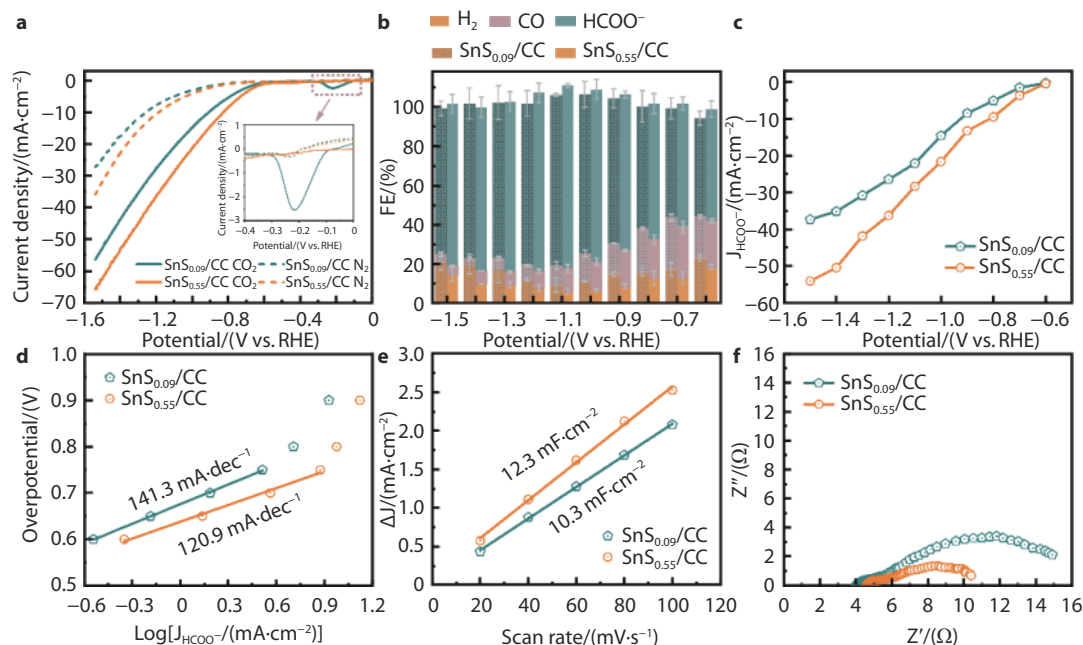

Fig. 3 **a**, Geometrical current densities over the SnS$_{0.09}$/CC and SnS$_{0.55}$/CC in CO$_2$- and N$_2$-saturated 0.5 M KHCO$_3$. **b**, Potential-dependent FEs of CO, H$_2$ and formate and **c**, partial current densities of formate (J$_{HCOO^-}$) over the SnS$_{0.09}$/CC and SnS$_{0.55}$/CC. **d**, Tafel plots of the SnS$_{0.09}$/CC and SnS$_{0.55}$/CC. **e**, Charging current density differences plotted against scan rates for the SnS$_{0.09}$/CC and SnS$_{0.55}$/CC. The fitting slopes are twice that of the Cdl values. **f**, Nyquist plots of the SnS$_{0.09}$/CC and SnS$_{0.55}$/CC at -0.8 V vs. RHE.

SnS$_{0.09}$/CC-12 h demonstrated that SnS$_{0.09}$/CC was reduced to Sn (Fig. S16e and S16f). Compared with SnS$_{0.55}$/CC, SnS$_{0.55}$/CC-12 h after 12-h stability test showed clear XRD diffraction peaks, but no obvious characteristic peak for metallic Sn was observed in the XPS spectra. The above characterization results indicated that the electrocatalysts continued to undergo in-situ transformation under the action of a long-time CO$_2$ reduction potential. Compared with other tin sulfide materials, SnS$_{0.09}$/CC and SnS$_{0.55}$/CC had comparable electrocatalytic properties and milder synthesis conditions (Table S5).

To further understand the different activities of SnS$_{0.09}$/CC and SnS$_{0.55}$/CC in CO$_2$ electroreduction, we investigated the relevant reaction kinetics. Fig. 3d showed the Tafel plots (overpotentials for formate production vs. log J$_{HCOO^-}$) of the two electrodes. The Tafel slopes of SnS$_{0.09}$/CC and SnS$_{0.55}$/CC were calculated to be 141.3 and 120.9 mV/dec, respectively. Theoretically, the Tafel slope of activation process is 118 mV/dec. The Tafel slopes of the two electrodes were both close to 118 mV/dec, proving that the activation of CO$_2$ serves as the rate-limiting step in the system of SnS$_x$.[30,37,43] The Cdl values of SnS$_{0.55}$/CC (12.3 mF/cm^2) was slightly larger than that of SnS$_{0.09}$/CC (10.3 mF/cm^2) (Fig. S21). Given that the Cdl value is positively correlated with the electrochemical active surface area (ECSA), the geometrical current density was normalized by Cdl values to evaluate the intrinsic activity of catalysts. The Cdl-normalized current density demonstrated that the different ECSA of the two catalysts brought by different potential regions of CV activation was not the main reason for the enhanced current density (Fig. S22). Further, Fig. 3f showed the Nyquist plots of the SnS$_{0.09}$/CC and SnS$_{0.55}$/CC. The charge transfer resistance of SnS$_{0.55}$/CC was smaller than that of SnS$_{0.09}$/CC, indicating a faster reaction rate.[30,37,43] Based on the above analysis, SnS$_{0.55}$/CC promoted the kinetics of CO$_2$ activation process in CO$_2$ electroreduction.

Discussion

It's found that the composition and morphology of SnS$_x$ chalcogel were affected by the regulation of CV activation, thus resulting in different performances for electrocatalytic CO$_2$RR. Using SnS$_x$ as a pre-catalyst, SnS$_{0.09}$/CC and SnS$_{0.55}$/CC were obtained through CV activation in different potential ranges. According to the characterizations, metal Sn was generated on the SnS$_{0.09}$/CC electrodes after CV activation. SnS$_{0.09}$/CC had less S contents than SnS$_{0.55}$/CC. Both electrodes showed high selectivity to formate in the electrocatalytic CO$_2$RR. SnS$_{0.55}$/CC had a higher current density and FE$_{HCOO^-}$ than SnS$_{0.09}$/CC. This phenomenon could be attributed to the different S content in SnS$_{0.09}$/CC and SnS$_{0.55}$/CC obtained by CV activation at different potential intervals. Being different from SnS$_{0.09}$/CC, the formation for SnS$_{0.55}$/CC underwent oxidation reactions with S ions, resulting in higher S content in SnS$_{0.55}$/CC. Different degrees of the peaks shift of Sn and S in XPS spectra and the reaction kinetics analysis indicated that the presence of more S affects the electronic structure of the catalysts and promotes the kinetics of CO$_2$ activation. There were also works that demonstrated that the presence of S enhanced the formation of formate.[46,49,50] The presence of S could weaken the HCOO* adsorption energies, thus favoring the formation of HCOO* toward formate.[47,49] In our work, although both electrodes still underwent transforma-

tion after 12-h stability test, FE$_{HCOO^-}$ could be maintained and SnS$_{0.55}$/CC outperformed SnS$_{0.09}$/CC. Our work sheds light on the effect of the CV activation process for the construction of "real" electrocatalysts for CO$_2$RR.

Conclusions

In conclusion, tin sulfide chalcogel was prepared by a simple and mild metathesis reaction and applied as the pre-catalyst for electrochemical CO$_2$RR. Tin sulfide chalcogel derived catalysts with different S contents were obtained through CV activation at different potential intervals, as the electrocatalysts underwent different redox processes. SnS$_{0.55}$/CC with higher S contents exhibited higher current density and a higher Faraday efficiency for formate than SnS$_{0.09}$/CC. The experimental results suggested that higher S content affected the interaction between the catalysts and CO$_2$, promoted CO$_2$ activation and favored the formation of formate. Our work revealed that different S contents of catalysts affected the performance of electrocatalytic CO$_2$RR, while the influence of the choice of potential intervals in CV activation on the electrocatalysts conversion also brought valuable insights for other electrocatalytic applications.

■ CONFLICT OF INTEREST

The authors declare no conflict of interest.

■ AUTHOR CONTRIBUTIONS

J. Liu conceived the idea and designed the experiments. J. Bai, L. Yang and J. Liu cowrote the paper. J. Bai synthesized and characterized the samples and further analyzed the results. J. Bai performed the catalytic tests. All authors discussed and commented on the manuscript.

■ REFERENCES

1. S. Bag, P. N. Trikalitis, P. J. Chupas, G. S. Armatas and M. G. Kanatzidis, *Science*, 2007, 317, 490
2. S. Bag, I. U. Arachchige and M. G. Kanatzidis, *J. Mater. Chem.*, 2008, 18, 3628
3. S. Bag, A. F. Gaudette, M. E. Bussell and M. G. Kanatzidis, *Nat. Chem.*, 2009, 1, 217
4. Y. Oh, S. Bag, C. D. Malliakas and M. G. Kanatzidis, *Chem. Mater.*, 2011, 23, 2447
5. K. Polychronopoulou, C. D. Malliakas, J. He and M. G. Kanatzidis, *Chem. Mater.*, 2012, 24, 3380
6. S. Chandrasekaran, L. Yao, L. Deng, C. Bowen, Y. Zhang, S. Chen, Z. Lin, F. Peng and P. Zhang, *Chem. Soc. Rev.*, 2019, 48, 4178
7. Y. Zhang, Y. Zhang, H. Zhang, L. Bai, L. Hao, T. Ma and H. Huang, *Coord. Chem. Rev.*, 2021, 448, 214147
8. K. S. Subrahmanyam, D. Sarma, C. D. Malliakas, K. Polychronopoulou, B. J. Riley, D. A. Pierce, J. Chun and M. G. Kanatzidis,

Chem. Mater., 2015, 27, 2619

9. Y. Shim, R. M. Young, A. P. Douvalis, S. M. Dyar, B. D. Yuhas, T. Bakas, M. R. Wasielewski and M. G. Kanatzidis, *J. Am. Chem. Soc.*, 2014, 136, 13371

10. K. S. Subrahmanyam, C. D. Malliakas, S. M. Islam, D. Sarma, J. Wu and M. G. Kanatzidis, *Chem. Mater.*, 2016, 28, 7744

11. B. D. Yuhas, C. Prasittichai, J. T. Hupp and M. G. Kanatzidis, *J. Am. Chem. Soc.*, 2011, 133, 15854

12. A. Banerjee, B. D. Yuhas, E. A. Margulies, Y. Zhang, Y. Shim, M. R. Wasielewski and M. G. Kanatzidis, *J. Am. Chem. Soc.*, 2015, 137, 2030

13. M. Shafaei-Fallah, A. Rothenberger, A. P. Katsoulidis, J. He, C. D. Malliakas and M. G. Kanatzidis, *Adv. Mater.*, 2011, 23, 4857

14. K. S. Subrahmanyam, I. Spanopoulos, J. H. Chun, B. J. Riley, P. K. Thallapally, P. N. Trikalitis and M. G. Kanatzidis, *ACS Appl. Mater. Interfaces*, 2017, 9, 33389

15. Z. Hassanzadeh Fard, S. M. Islam and M. G. Kanatzidis, *Chem. Mater.*, 2015, 27, 6189

16. B. J. Riley, J. Chun, W. Um, W. C. Lepry, J. Matyas, M. J. Olszta, X. Li, K. Polychronopoulou and M. G. Kanatzidis, *Environ. Sci. Technol.*, 2013, 47, 7540

17. J. Liu, K. He, W. Wu, T. B. Song and M. G. Kanatzidis, *J. Am. Chem. Soc.*, 2017, 139, 2900

18. B. D. Yuhas, A. L. Smeigh, A. P. Samuel, Y. Shim, S. Bag, A. P. Douvalis, M. R. Wasielewski and M. G. Kanatzidis, *J. Am. Chem. Soc.*, 2011, 133, 7252

19. J. Staszak-Jirkovsky, C. D. Malliakas, P. P. Lopes, N. Danilovic, S. S. Kota, K. C. Chang, B. Genorio, D. Strmcnik, V. R. Stamenkovic, M. G. Kanatzidis and N. M. Markovic, *Nat. Mater.*, 2016, 15, 197

20. X. Shan, J. Liu, H. Mu, Y. Xiao, B. Mei, W. Liu, G. Lin, Z. Jiang, L. Wen and L. Jiang, *Angew Chem. Int. Ed.*, 2020, 59, 1659

21. H. Mu, G. Lin, Y. Zhang, Y. Xiao and J. Liu, *Colloids Surf. A Physicochem. Eng. Asp.*, 2021, 623, 126734

22. G. Wang, J. Chen, Y. Ding, P. Cai, L. Yi, Y. Li, C. Tu, Y. Hou, Z. Wen and L. Dai, *Chem. Soc. Rev.*, 2021, 50, 4993

23. Y. Y. Birdja, E. Pérez-Gallent, M. C. Figueiredo, A. J. Göttle, F. Calle-Vallejo and M. T. M. Koper, *Nat. Energy*, 2019, 4, 732

24. M. G. Kibria, J. P. Edwards, C. M. Gabardo, C. T. Dinh, A. Seifitokaldani, D. Sinton and E. H. Sargent, *Adv. Mater.*, 2019, 31, 1807166

25. S. A. Patil, H. T. Bui, S. Hussain, I. Rabani, Y. Seo, J. Jung, N. K. Shrestha, H. Kim and H. Im, *Dalton Trans.*, 2021, 50, 12723

26. S. A. Patil, N. K. Shrestha, A. I. Inamdar, C. Bathula, J. Jung, H. Im and H. Kim, *Int. J. Energy Res.*, 2022

27. S. A. Patil, N. K. Shrestha, S. Hussain, J. Jung, S. W. Lee, C. Bathula, A. N. Kadam, H. Im and H. Kim, *J. Hazard. Mater.*, 2021, 417, 126105

28. W. Yu, F. Shu, Y. Huang, F. Yang, Q. Meng, Z. Zou, J. Wang, Z. Zeng, G. Zou and S. Deng, *J. Mater. Chem. A*, 2020, 8, 20677

29. M. Chen, S. Wan, L. Zhong, D. Liu, H. Yang, C. Li, Z. Huang, C. Liu, J. Chen, H. Pan, D. S. Li, S. Li, Q. Yan and B. Liu, *Angew Chem. Int. Ed.*, 2021, 60, 26233

30. A. Zhang, Y. Liang, H. Li, S. Wang, Q. Chang, K. Peng, Z. Geng and J. Zeng, *Nano Lett.*, 2021, 21, 7789

31. S. Zhao, S. Li, T. Guo, S. Zhang, J. Wang, Y. Wu and Y. Chen, *Nano-Micro Lett.*, 2019, 11, 62

32. F. Wei, T. Wang, X. Jiang, Y. Ai, A. Cui, J. Cui, J. Fu, J. Cheng, L. Lei, Y. Hou and S. Liu, *Adv. Funct. Mater.*, 2020, 30, 2002092

33. W. Ni, Y. Gao, Y. Lin, C. Ma, X. Guo, S. Wang and S. Zhang, *ACS Catal.*, 2021, 11, 5212

34. Z. Wu, H. Wu, W. Cai, Z. Wen, B. Jia, L. Wang, W. Jin and T. Ma, *Angew Chem. Int. Ed.*, 2021, 60, 12554

35. Y. J. Ko, J. Y. Kim, W. H. Lee, M. G. Kim, T. Y. Seong, J. Park, Y. Jeong, B. K. Min, W. S. Lee, D. K. Lee and H. S. Oh, *Nat. Commun.*, 2022, 13, 2205

36. X. Zhang, M. Jiao, Z. Chen, X. Ma, Z. Wang, N. Wang, X. Zhang and L. Liu, *Chem. Eng. J.*, 2022, 429, 132145

37. Z. Chen, X. Zhang, M. Jiao, K. Mou, X. Zhang and L. Liu, *Adv. Energy Mater.*, 2020, 10, 1903664

38. G. A. El-Nagar, A. M. Mohammad, M. S. El-Deab and B. E. El-Anadouli, *ACS Appl. Mater. Interfaces*, 2017, 9, 19766

39. F. Joo, *ChemSusChem*, 2008, 1, 805

40. Q.-L. Zhu and Q. Xu, *Energy Environ. Sci.*, 2015, 8, 478

41. Q. Gong, P. Ding, M. Xu, X. Zhu, M. Wang, J. Deng, Q. Ma, N. Han, Y. Zhu, J. Lu, Z. Feng, Y. Li, W. Zhou and Y. Li, *Nat. Commun.*, 2019, 10, 2807

42. S. Bag and M. G. Kanatzidis, *J. Am. Chem. Soc.*, 2010, 132, 14951

43. A. Zhang, R. He, H. Li, Y. Chen, T. Kong, K. Li, H. Ju, J. Zhu, W. Zhu and J. Zeng, *Angew Chem. Int. Ed.*, 2018, 57, 10954

44. F. Li, L. Chen, M. Xue, T. Williams, Y. Zhang, D. R. MacFarlane and J. Zhang, *Nano Energy*, 2017, 31, 270

45. B. Ni, T. He, J. O. Wang, S. Zhang, C. Ouyang, Y. Long, J. Zhuang and X. Wang, *Chem. Sci.*, 2018, 9, 2762

46. X. Zheng, P. De Luna, F. P. García de Arquer, B. Zhang, N. Becknell, M. B. Ross, Y. Li, M. N. Banis, Y. Li, M. Liu, O. Voznyy, C. T. Dinh, T. Zhuang, P. Stadler, Y. Cui, X. Du, P. Yang and E. H. Sargent, *Joule*, 2017, 1, 794

47. T. Shinagawa, G. O. Larrazábal, A. J. Martín, F. Krumeich and J. Pérez-Ramírez, *ACS Catal.*, 2018, 8, 837

48. Y. Zhang, L. Hu and W. Han, *J. Mater. Chem. A*, 2018, 6, 23610

49. Y. Deng, Y. Huang, D. Ren, A. D. Handoko, Z. W. Seh, P. Hirunsit and B. S. Yeo, *ACS Appl. Mater. Interfaces*, 2018, 10, 28572

50. W. Ma, S. Xie, X. G. Zhang, F. Sun, J. Kang, Z. Jiang, Q. Zhang, D. Y. Wu and Y. Wang, *Nat. Commun.*, 2019, 10, 892